The Ice-Ocean governor: ice-ocean stress feedback limits Beaufort Gyre spin up

Gianluca Meneghello*[1], John Marshall[1], Jean-Michel Campin[1], Edward Doddridge[1], Mary-Louise Timmermans[2]

[1]Department of Earth, Atmospheric and Planetary Sciences, MIT, Cambridge, Massachusetts, USA

[2]Department of Geology and Geophysics, Yale University, New Haven, Connecticut, USA

*e-mail: gianluca.meneghello@gmail.com

April 6, 2018

Abstract

The Beaufort Gyre is a key circulation system of the Arctic Ocean and the main reservoir of freshwater within it. Storage and release of its freshwater not only has significant implications for the fate of Arctic sea ice cover, but also to climate in the North Atlantic and globally. We present a new mechanism that is fundamental to the dynamics of the Arctic and its ability to store fresh water, namely the "ice-ocean governor". Wind blows over the ice and the ice drags the ocean along with it. But as the gyre spins up, surface currents catch the ice up and effectively turn off the Ekman pumping. This governor sets the basic properties of the gyre, such as its depth, freshwater content, and strength. Analytical and numerical modeling is employed to demonstrate the mechanism, contrasting equilibration processes in an ice-covered versus ice-free gyre. Observations are presented and interpreted in terms of the governor mechanism. Our study has significant consequences for freshwater accumulation and release in a warming climate with continued sea-ice losses. We argue that reduced sea-ice extent and more mobile ice will result in the gyre becoming deeper and accumulating more freshwater which will ultimately be released by instability of the gyre.

1 Introduction

Anticyclonic winds centered over the Arctic Ocean's Beaufort Gyre (BG) force a lateral Ekman transport bringing surface freshwater towards the center of the gyre and driving it downwards. This convergence increases the freshwater content of the BG and spins up the geostrophic current [1–5]. Freshwater accumulation, storage and release from the BG, controlled by these wind-driven dynamics, have far-reaching influence on Arctic and global climate [4]. However, wind variability alone cannot completely explain the variability in freshwater content [6]: gyre spin up and freshwater increase, proportional to the curl of the ocean surface stress, are complicated by the presence of sea ice cover, which mediates wind forcing on the ocean [7–11]. Here we show how a previously unconsidered interaction between under-ice geostrophic ocean currents and sea-ice cover (an *ice-ocean stress governor*) plays a key role in regulating the strength and sign of the ice-ocean stress curl, and in equilibrating the freshwater content of the BG.

The total stress $\boldsymbol{\tau}$ at the ocean surface is a combination of ice-ocean stress $\boldsymbol{\tau}_i$ and air-ocean stress $\boldsymbol{\tau}_a$, each of which may be estimated by a quadratic drag law, weighted by the

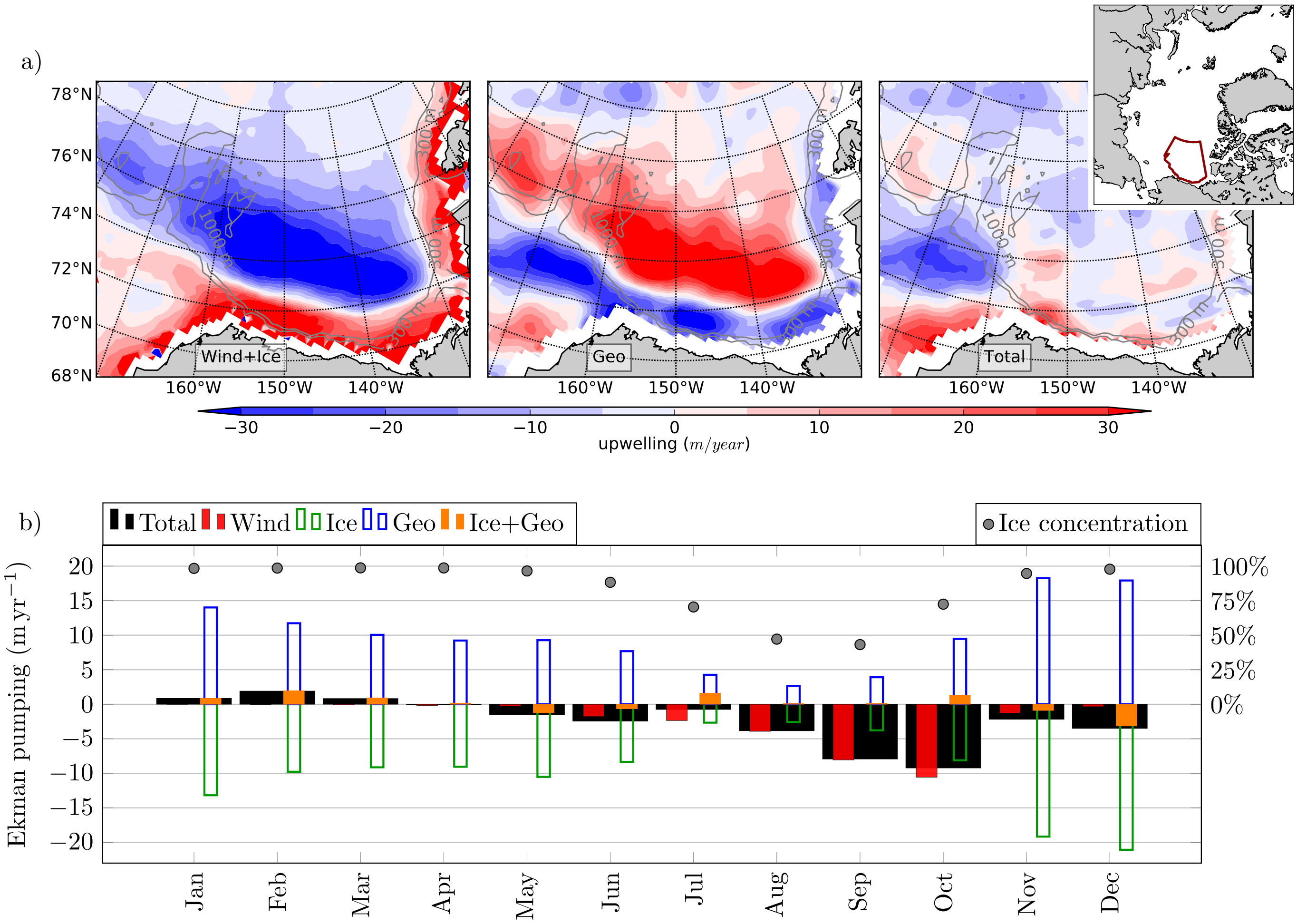

Figure 1. Ekman pumping climatology. (a) Mean Ekman pumping over 2003-2014; negative (blue) indicates downwelling, positive (red) upwelling. Left: downwelling estimates locally exceed 30 $\mathrm{m\,yr^{-1}}$ if the geostrophic current is neglected; center: inclusion of the geostrophic current results in an upwelling effect, largely compensating the ice-driven downwelling; right: the net Ekman pumping, the sum of the previous two panels, yields only moderate downwelling together with patches of upwelling. The BG Region (BGR) is marked by a red line in the inset. (b) Monthly Ekman pumping climatology over the BGR and its partitioned contributions, where negative indicates downwelling. Black bars show total Ekman pumping, equivalent to the right panel in a). Red and orange bars show pumping induced by winds over ice-free regions, and by ice in ice-covered regions respectively. Within ice-covered regions, empty green bars show downwelling induced by the ice if the geostrophic current is neglected, while blue bars show upwelling induced by the geostrophic currents flowing under the sea ice. Blue and green bars largely balance each another, and exactly balance if $\boldsymbol{u}_{rel}$=0. Grey dots represent ice concentration.

sea-ice concentration α [12]:

$$\boldsymbol{\tau} = \alpha \underbrace{\rho C_{Di} \left|\boldsymbol{u}_{rel}\right| (\boldsymbol{u}_{rel})}_{\boldsymbol{\tau}_i} + (1-\alpha) \underbrace{\rho_a C_{Da} \left|\boldsymbol{u}_a\right| (\boldsymbol{u}_a)}_{\boldsymbol{\tau}_a}. \tag{1}$$

C_{Di} and C_{Da} are drag coefficients for the ice-ocean and air-ocean stress respectively, ρ is water density, and ρ_a is air density. In the computation of $\boldsymbol{\tau}_a$, the surface ocean velocity, of a few cm s^{-1}, is considered negligible with respect to a wind velocity $\boldsymbol{u}_a$ of a few m s^{-1}. On the other hand, surface ocean velocity cannot be neglected in the estimation of $\boldsymbol{\tau}_i$. The ice-ocean relative velocity $\boldsymbol{u}_{rel}$ is expressed as the difference between the ice velocity $\boldsymbol{u}_i$ and the surface ocean velocity, taken to be the sum of geostrophic $\boldsymbol{u}_g$ and ageostrophic (Ekman) $\boldsymbol{u}_e$ components. That is $\boldsymbol{u}_{rel} = \boldsymbol{u}_i - (\boldsymbol{u}_g + \boldsymbol{u}_e)$.

Observations of wind, ice velocity, surface current and ice concentration allow estimates of $\boldsymbol{\tau}$, which may be used to produce climatologies of the Ekman pumping rate $w_{Ek} = \nabla \times (\frac{\boldsymbol{\tau}}{\rho f})$ in the BG Region, (BGR, Figure 1), where f is the Coriolis parameter. The intensity of the ocean surface currents plays a central role in modulating the Ekman pumping in an ice covered gyre [8–11]. Estimates of wind- and ice-induced downwelling locally exceeds 30 m yr^{-1} if the geostrophic current is neglected (Figure 1a, blue region in the left panel, see also [12, 13]). This is largely compensated by the upwelling effect of the surface current flowing below the ice (red region in the central panel), acting as a negative feedback and turning off the downwelling. That is, the governor drives the system towards $\boldsymbol{u}_{rel} = 0$. Consequently the net Ekman pumping is strongly reduced (right panel). A monthly climatology of Ekman pumping and its components averaged over the BGR (Figure 1b) shows how the total Ekman pumping is reduced by the geostrophic current, and even reversed during the months of January, February and March [11].

We demonstrate here how the governor acts as a mechanism to equilibrate the freshwater content of the gyre. For example, should the anticyclonic ice stress curl — and freshwater accumulation rate — intensify, the geostrophic flow of the gyre will strengthen until the governor "kicks in" and reduces the surface stress and freshwater accumulation rate. This is a distinct alternative to the eddy-equilibration mechanism first proposed for the southern ocean [14, 15], and more recently extended to the BG [7, 8, 16–19]. To explore the governor mechanism, we start by analyzing the response of an idealized gyre under two different limit-case scenarios: i) an ice-driven gyre (α=1, in which forcing depends purely on gradients of $\boldsymbol{\tau} = \boldsymbol{\tau}_i$) and ii) an ice free, wind-driven gyre (α=0, in which forcing depends purely on gradients of $\boldsymbol{\tau} = \boldsymbol{\tau}_a$). We then proceed by discussing observations of Ekman pumping, Dynamic Ocean Topography (DOT) and freshwater content anomaly (FWC) in the BG over the last decade or so, in terms of the ice governor mechanism. We conclude by speculating on the role of the governor in a warming world characterized by an increasingly ice free Arctic Ocean.

2 The ice-ocean stress governor

We run numerical experiments employing a high resolution idealized model of the BG based on the MIT General Circulation Model [20, 21] and designed to capture both mesoscale eddy processes and the ice-ocean governor mechanism (see Supplementary material), and then compare the numerical results with a simple analytical model capturing the essential components of the ice-ocean governor. All simulations begin with a uniformly-stratified ocean at rest in which freshwater is pumped down through the action of either a wind-driven or an ice-driven surface stress. The ocean is spun up via a steady axisymmetric, anticyclonic, wind/ice field with zero speed at the center of the domain and reaching a maximum at a radius of 300 km (see Figure A.1), broadly consistent with observations [11]. Wind and ice velocity magnitudes are chosen to produce the same surface stress $\boldsymbol{\tau}_0$ when the ocean is at rest. The stress, and hence the freshwater accumulation rate, remains constant in the ice-free case α=0, but evolves and, in fact, diminishes in time in the ice-driven case α=1 as the surface currents spin up to match the ice speed. Five experiments are run for each scenario, varying ice and wind velocities; we diagnose the gyre response by computing the maximum depth anomaly h of the $S = 31$ isohaline and the change in freshwater content (see Supplementary material) stored in the gyre (Figure 2).

2.1 Ice-driven gyre ($\alpha = 1$): stress-equilibrated

We begin by describing the evolution of a typical ice-covered simulation in which the ice governor operates (Figure 2a, left panel and Figure 2b, thick blue line). Ice-covered experiments have imposed anticyclonic ice drift with a range of maximum speeds broadly in agreement with observations [11]; our example simulation has an ice-speed maximum of $8\,\mathrm{cm\,s^{-1}}$, corresponding to a surface stress $\tau_0 = 0.04\,\mathrm{N\,m^{-2}}$. Initially, the ocean is at rest and the applied surface stress gives rise to an Ekman pumping of order $w_{Ek} \approx \tau_0/(\rho f R) \approx 30\,\mathrm{m\,yr^{-1}}$, where $R \approx 300\,\mathrm{km}$ is the radius of the gyre and $f = 1.45 \times 10^{-4}\,\mathrm{s^{-1}}$. As time progresses, surface freshwater is accumulated towards the center of the gyre and pumped downwards inflating isohalines, and a geostrophic current is spun up; by year 10, the ocean

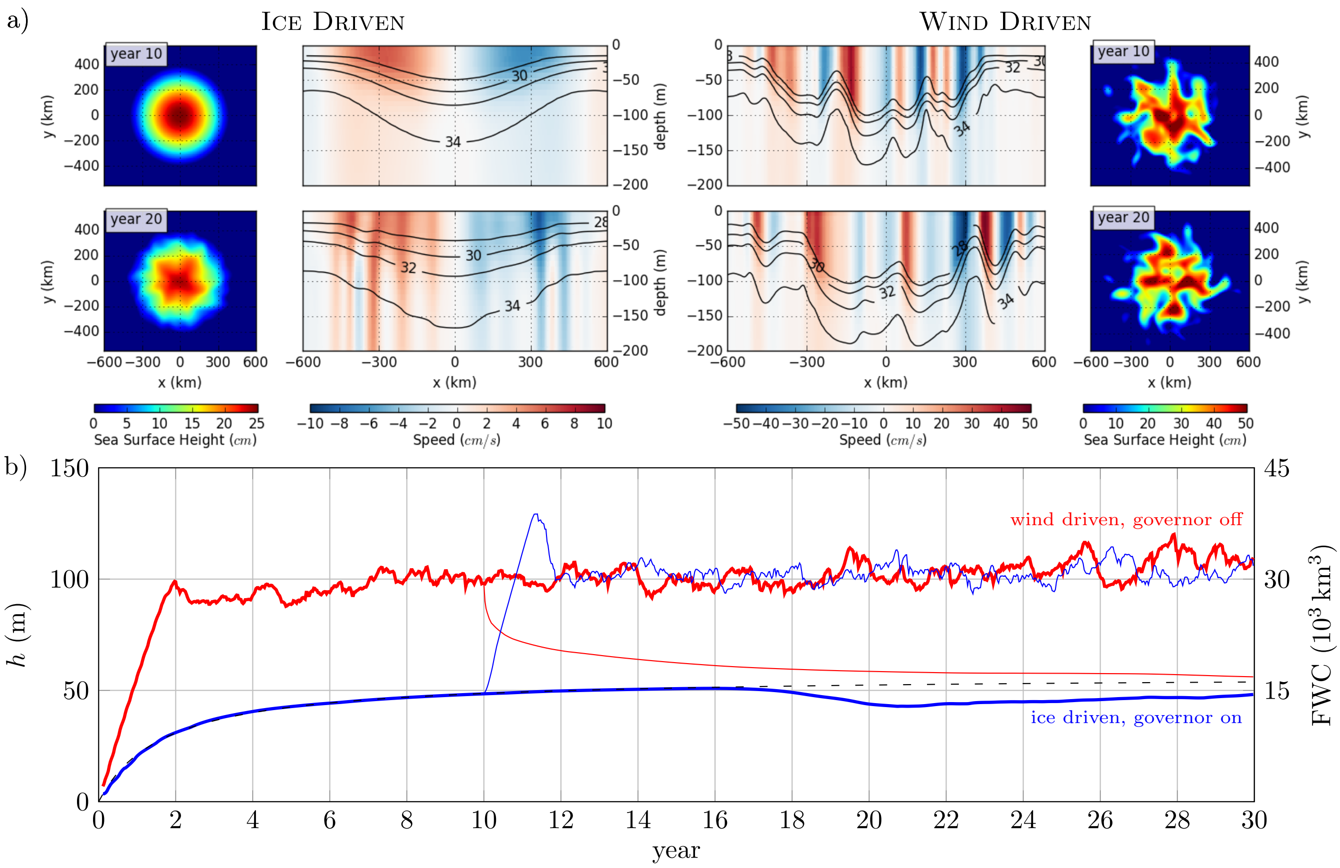

Figure 2. (a) Instantaneous sea surface height (exterior panels), vertical section of salinity (central panels, black contours) and speed (central panels, color) at years 10 (top row) and 20 (bottom row) for the ice-driven (α=1 and $u_i = 8\,\mathrm{cm\,s^{-1}}$, left) and the wind-driven (α=0 and $u_a = 4.8\,\mathrm{m\,s^{-1}}$, right) scenarios. Note the different ranges (color scales) between the two cases. Only the top 200 m of the 800 m domain depth are shown in the central panels. (b) Depth anomaly h of the 31 isohaline, and equivalent freshwater content anomaly (FWC, right axis), for the ice driven $\alpha = 1$ (blue) and wind driven $\alpha = 0$ (red) scenario. For α=1, Ekman pumping spins up the gyre until the surface ocean speed approaches the ice-drift speed (such that $\boldsymbol{u}_{rel}$ approaches 0), thus turning off the ice-ocean stress driving spin up. The dashed black line is a fit of equation (6), and is indistinguishable from the numerical solution before year 16. Evidence of weak baroclinic instability is visible in the later stages of the evolution (around year 20). For α=0, the gyre inflates at a constant rate proportional to the Ekman pumping until it reaches a quasi-equilibrium in which Ekman pumping is balanced by baroclinic instability and lateral eddy fluxes out of the gyre. Thin lines in panel b) show the transition between an ice-covered and an ice-free state (blue), and vice versa (red).

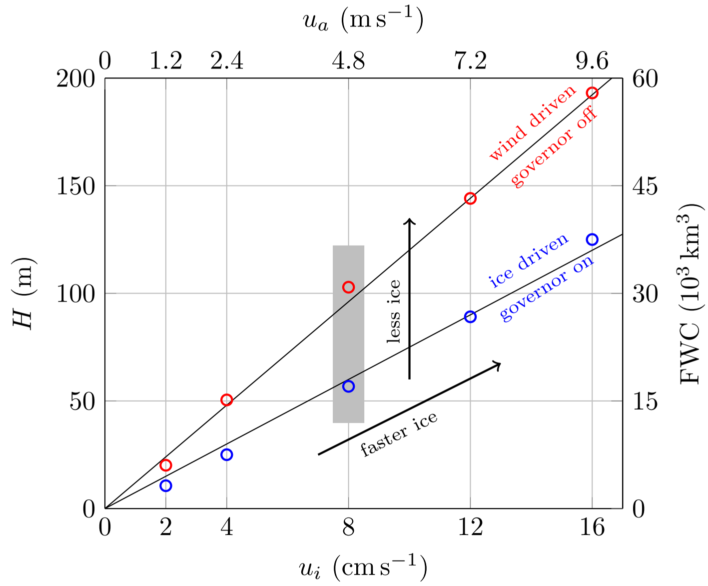

Figure 3. Asymptotic depth anomaly H, and equivalent freshwater content anomaly (FWC, right axis), for 5 different model runs each of the wind-driven (H_K, red) and ice-driven (H_τ, blue) scenarios, as a function of the wind and ice velocity respectively. Black lines show the theoretical prediction from equation (5) for the ice driven (blue) scenario, and the least-squares fit for the wind driven (red) scenario. The gray area marks the example cases shown in Figure 2. Arrows show two possible mechanisms for altering the depth and freshwater content of the gyre: an increase of the ice speed — faster ice — and the turning off of the ice-ocean governor due to a reduced ice cover — less ice.

surface speed is approximately equal to the ice-drift speed (Figure 2a, top row). After 10-15 years h stabilizes at a depth of around 50 m, and the freshwater content anomaly equilibrates at a maximum of around 15 000 km^3 (Figure 2b, thick blue line). Weak baroclinic instability develops around year 20, but the ice-ocean stress governor is sufficiently efficient in the ice-covered scenario that baroclinic instability does not play any appreciable role in gyre equilibration. We remark that the time at which baroclinic instability develops depends on the gyre depth, and finally on the ice velocity.

To develop a conceptual model, we assume that the isopycnal depth anomaly h increases at a rate proportional to w_{Ek}, which in the ice-driven case is proportional to the curl of the surface stress $\boldsymbol{\tau}_i$, and thus depends on the geostrophic velocity $\boldsymbol{u}_g$ via equation (1). We may then write

$$\frac{dh}{dt} = \frac{\gamma}{\rho f}\frac{\tau_i}{R}, \tag{2}$$

where γ is a dimensionless constant that depends on the spatial distribution of the Ekman pumping and the geometry of the isopycnal slope.

In order to obtain an analytical solution which enables us to identify controlling parameters, we make the following approximations. First, the Ekman velocity u_e may be reasonably neglected in estimating τ_i as, at first order, it can be considered itself a linear function of $\boldsymbol{u}_i - \boldsymbol{u}_g$ and thus absorbed by the constant γ. Second, we suppose the bottom current to be negligible so that the magnitude of the surface geostrophic velocity may be estimated by the thermal wind relationship as follows

$$u_g \sim \frac{g'}{f}\frac{h}{R}, \tag{3}$$

where $g' = g\Delta\rho/\rho$ is the reduced gravity and $\Delta\rho$ is the vertical density difference between the top and bottom of the model domain. The close agreement between theory and simulation, reported below, attests to the validity of these approximations.

With equation (3) and (1), equation (2) may be expressed as

$$\frac{dh}{dt} = \frac{H_\tau}{T_\tau}\left(1 - \frac{h}{H_\tau}\right)^2, \tag{4}$$

where

$$H_\tau = \frac{f}{g'}Ru_i \quad \text{and} \quad T_\tau = \frac{(fR)^2}{\gamma g' C_{Di} u_i} \tag{5}$$

are ice-stress-equilibrated length and time scales respectively and we have taken $h < H_\tau$ (equivalent to $u_g < u_i$) to remove the absolute value from equation (1). The scale H_τ is the stress-equilibrated steady-state isopycnal depth (i.e., $dh/dt = 0$ when $h = H_\tau$). It can be seen from equation (3) and (5) that $h = H_\tau$ is equivalent to $u_g = u_i$ (i.e., $u_{rel} = 0$). In this limit the gyre has been equilibrated by the ice-ocean stress governor. Equation (4), with $h(t = 0) = 0$, has solution

$$h = H_\tau\left(\frac{t}{t + T_\tau}\right). \tag{6}$$

Values of H_τ are obtained by fitting equation (6) to each simulation, and show a linear dependence on u_i as expected from equation (5) (Figure 3, blue circles).

2.2 Wind-driven gyre (α=0): eddy-equilibrated

The reference wind driven experiment (Figure 2a, right, and Figure 2b, thick red line) has an imposed anticyclonic wind-speed maximum of 4.8 m s^{-1}, corresponding to a surface stress of $\tau_a = 0.04\,\mathrm{N\,m^{-2}}$, equivalent to the initial stress in the ice-driven scenario. Initially, the depth of the gyre (diagnosed by h) and its freshwater content increase linearly at a constant rate proportional to the vertical Ekman pumping of order $w_{Ek} \approx \tau_a/(\rho f R) \approx 30\,\mathrm{m\,yr^{-1}}$ (Figure 2b, thick red line). The linear increase in h proceeds until baroclinic instability develops. By year 2 of the simulation, $h \approx 100$ m and the freshwater content anomaly reaches $30\,000\,\mathrm{km}^2$, or twice the asymptotic values of the ice-driven scenario despite the initial spin-up rate being the same. Baroclinic instability ultimately arrests the deepening with eddy fluxes transporting freshwater laterally out of the gyre (Figure 2a, right). The gyre then reaches a quasi-steady equilibrium characterized by an active eddy field, and a balance between Ekman downwelling and eddy fluxes [8, 17, 18].

The statistically steady equilibrium state of the gyre can be described as a balance between the mean (Eulerian) overturning streamfunction (proportional to surface wind stress), and the eddy overturning streamfunction [15, 22, 23]. This *vanishing residual-mean* circulation framework [8] yields the following scaling for the equilibrated value of h:

$$H_K \sim \frac{R}{\rho f K}\tau_a = \frac{R}{\rho f K}\rho_a C_{Da} u_a^2 = u_a R \sqrt{\frac{\rho_a C_{Da}}{\rho f \kappa}}, \tag{7}$$

where K is eddy diffusivity and the subscript K implies eddy equilibrated. The final equality assumes a linear relationship between eddy diffusivity and isopycnal slope, $K = \kappa H_K/R$ (for some constant κ). The linear relationship between u_a and equilibrated isopycnal depth H_K implied by equation (7) is clear over the range of imposed u_a in the five wind-driven simulations (Figure 3, red circles).

Finally we carry out two experiments to examine the effect of a sudden transition between an ice-covered and an ice-free gyre. The eddying, deeper halocline transitions rapidly to a non-eddying solution when the governor is turned on by adding the ice cover (Figure 2b, thin red line). The shallower, non-eddying solution transitions to an eddying solution when the governor is turned off by removing the ice cover (Figure 2b, thin blue line). Approximately $15\,000\,\mathrm{km}^3$ of freshwater is released or accumulated during the process.

3 Implications of the ice-governor

We have analyzed and compared two different mechanisms governing the equilibration of the Beaufort Gyre. In the wind driven scenario in the absence of ice, the depth and freshwater content of the gyre is governed by the balance between Ekman pumping accumulating surface freshwater and a vigorous eddy field releasing it by baroclinic instability. This has been previously hypothesized to play a central role in gyre equilibration [8, 17]. Here we have introduced another fundamental mechanism, namely the ice-ocean stress governor, a negative feedback between the ice-mediated Ekman pumping and the surface geostrophic currents of the gyre. We have demonstrated how, in an ice-driven gyre, the spin up of the gyre, its isopycnal depth anomaly and its freshwater content, can be regulated by the interaction between the sea-ice and the surface geostrophic current flowing at comparable speeds. In this new scenario, the regulating mechanism drives freshwater accumulation rate to zero rather than releasing the accumulated freshwater by eddy transport.

We have considered either completely ice covered ($\alpha = 1$) or ice free ($\alpha = 0$) scenarios. It has to be remarked that the case of low ice concentrations, when ice is free-drifting, is nearly equivalent to the wind driven case. By contrast, the case of completely immobile ice would shield the underlying ocean from the winds above and result in the anticyclonic gyre spinning down, upwelling and divergence of freshwater out of the gyre through surface Ekman processes.

Evidence of the role of the ice-ocean governor can be seen by comparing the Ekman pumping climatology and Dynamic Ocean Topography (DOT) or, equivalently, freshwater content anomaly (FWC) [24] during the 2003-2014 observational period (Figure 4). Ice-driven downwelling is approximately balanced by the geostrophic-flow-driven upwelling over the entire record (empty green and blue bars respectively). The largest increase in DOT and FWC takes place in late 2007 [24, 25]; we argue that two different Ekman pumping regimes characterize the gyre before and after 2007-2008. In 2007, strong anticyclonic winds (red bars) acting on a largely ice free gyre (thick grey curve) increased its freshwater content by approximately 5000 km^3, or about a third of the 15 000 km^3 accumulated by our idealized model when the ice cover was removed (thin blue line in Figure 2b). The associated transition from a slow to a fast gyre [26] is reflected in the change from a downwelling- to an upwelling-favorable Ekman pumping regime for the ice covered regions (orange bars), despite an always downwelling favorable Ekman pumping in the ice free regions (red bars). This is the case until 2012, when, in addition to the usual wintertime current driven upwelling, cyclonic winds in summer [11, 27] result in a temporary reduction in the gyre DOT and freshwater content; the system returns towards the 2009-2011 equilibrium in the following years. We remark that the 2012 ice component (green empty bar) is still downwelling favorable despite cyclonic winds in the annual mean; indeed the total Ekman pumping would also be downward if it were not for the geostrophic current driving a strong upwelling in the ice covered region of the gyre. Clearly the ice-ocean governor plays an important role in stabilizing the gyre.

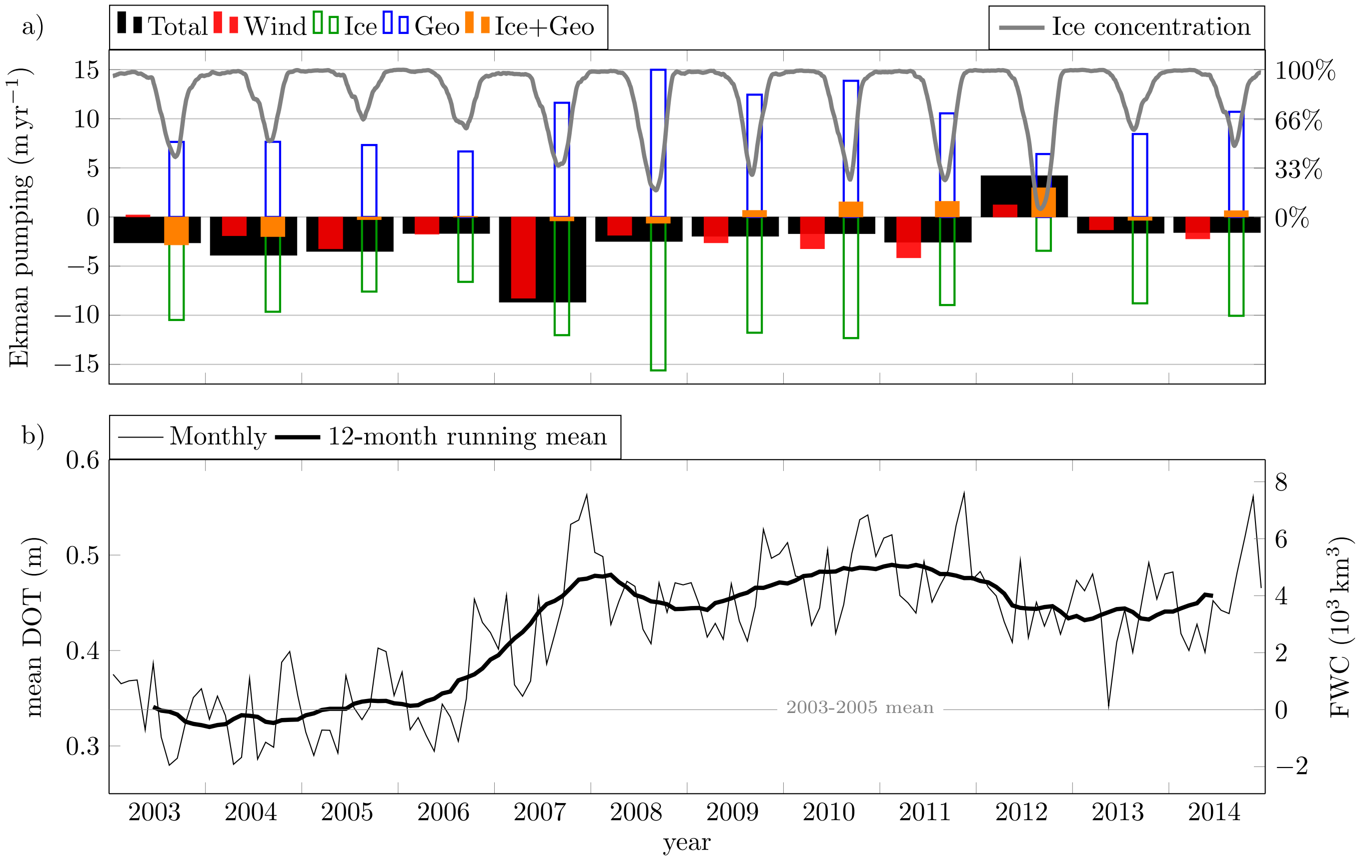

Figure 4. a) Yearly Ekman pumping climatology over the BGR, bars as in Figure 1b; mean ice concentration is shown by the gray thick line. b) Mean Dynamic Ocean Topography (DOT) [24] and freshwater content anomaly (FWC) with respect to the 2003-2005 mean (right axis) over the BGR.

In conclusion, the equilibrium of the gyre can be disrupted in two ways, as summarized by the arrows in Figure 3: a change in the wind or ice velocity, as suggested by previous authors [6], or a change in the effectiveness of the ice-ocean governor, as shown here. This suggests the potential for an important shift in BG dynamics under projected continued summer sea-ice decline in the coming years and decades. Increased summer Ekman downwelling will result in a deeper gyre, faster geostrophic currents and a more intense eddy field, while the faster geostrophic currents will drive a strong upwelling during the ice-covered winter: depending on gyre response timescales, a stronger seasonal cycle and spatial variability in isopycnal depth is to be expected, with the ice-ocean governor effectiveness changing with the evolving ice cover. This will in turn impact the dynamics of the halocline that insulates the ice-cover from warmer waters at depth, and hence the persistence of the ice-cover itself.

Acknowledgements

The authors thankfully acknowledge support from NSF Polar Programs, both Arctic and Antarctic.

Author contributions

All authors contributed equally to this study.

Additional information

The authors declare no competing financial interests.

References

1. Proshutinsky, A. Y. & Johnson, M. A. Two circulation regimes of the wind-driven Arctic Ocean. *Journal of Geophysical Research: Oceans* **102,** 12493–12514 (1997).
2. Proshutinsky, A., Bourke, R. H. & McLaughlin, F. A. The role of the Beaufort Gyre in Arctic climate variability: Seasonal to decadal climate scales. *Geophysical Research Letters* **29,** 15–1 (2002).
3. Proshutinsky, A. *et al.* Beaufort Gyre freshwater reservoir : State and variability from observations. *Journal of Geophysical Research* **114,** 1–25 (2009).

4. Proshutinsky, A., Dukhovskoy, D., Timmermans, M.-l., Krishfield, R. & Bamber, J. L. Arctic circulation regimes. *Philosophical transactions. Series A, Mathematical, physical, and engineering sciences* **373,** 20140160 (2015).
5. Timmermans, M. L. *et al.* Surface freshening in the Arctic Ocean's Eurasian Basin: An apparent consequence of recent change in the wind-driven circulation. *Journal of Geophysical Research: Oceans* **116** (2011).
6. Giles, K. A., Laxon, S. W., Ridout, A. L., Wingham, D. J. & Bacon, S. Western Arctic Ocean freshwater storage increased by wind-driven spin-up of the Beaufort Gyre. *Nature Geoscience* **5,** 194–197 (2012).
7. Davis, P. E. D., Lique, C. & Johnson, H. L. On the link between arctic sea ice decline and the freshwater content of the beaufort gyre: Insights from a simple process model. *Journal of Climate* **27,** 8170–8184 (2014).
8. Meneghello, G., Marshall, J., Cole, S. T. & Timmermans, M.-L. Observational inferences of lateral eddy diffusivity in the halocline of the Beaufort Gyre. *Geophysical Research Letters* **44** (Nov. 2017).
9. Zhong, W., Steele, M., Zhang, J. & Zhao, J. Greater Role of Geostrophic Currents in Ekman Dynamics in the Western Arctic Ocean as a Mechanism for Beaufort Gyre Stabilization. *Journal of Geophysical Research: Oceans* (Jan. 2018).
10. Dewey, S. *et al.* Arctic Ice-Ocean Coupling and Gyre Equilibration Observed With Remote Sensing. *Geophysical Research Letters* (Feb. 2018).
11. Meneghello, G., Marshall, J., Timmermans, M. L. & Scott, J. Observations of seasonal upwelling and downwelling in the Beaufort Sea mediated by sea ice. *J. Phys. Oceanogr.* **in press** (2018).
12. Yang, J. Seasonal and interannual variability of downwelling in the Beaufort Sea. *J Geophys Res* **114,** C00A14 (2009).
13. Yang, J. The seasonal variability of the Arctic Ocean Ekman transport and its role in the mixed layer heat and salt fluxes. *Journal of Climate* **19,** 5366–5387 (2006).
14. Karsten, R., Jones, H. & Marshall, J. The Role of Eddy Transfer in Setting the Stratification and Transport of a Circumpolar Current. *Journal of Physical Oceanography* **32,** 39–54 (2002).
15. Marshall, J. & Radko, T. Residual-Mean Solutions for the Antarctic Circumpolar Current and Its Associated Overturning Circulation. *Journal of Physical Oceanography* **33,** 2341–2354 (2003).

16. Lique, C., Johnson, H. L. & Davis, P. E. D. On the Interplay between the Circulation in the Surface and the Intermediate Layers of the Arctic Ocean. *Journal of Physical Oceanography* **45,** 1393–1409 (2015).

17. Manucharyan, G. E., Spall, M. A. & Thompson, A. F. A Theory of the Wind-Driven Beaufort Gyre Variability. *Journal of Physical Oceanography,* 3263–3278 (2016).

18. Manucharyan, G. E. & Spall, M. A. Wind-driven freshwater buildup and release in the Beaufort Gyre constrained by mesoscale eddies. *Geophysical Research Letters* **43,** 273–282 (2016).

19. Yang, J., Proshutinsky, A. & Lin, X. Dynamics of an idealized Beaufort Gyre: 1. the effect of a small beta and lack of western boundaries. *Journal of Geophysical Research: Oceans* **121,** 1249–1261 (2016).

20. Marshall, J., Adcroft, A., Hill, C., Perelman, L. & Heisey, C. A finite-volume, incompressible Navier Stokes model for studies of the ocean on parallel computers. *Journal of Geophysical Research: Oceans* **102,** 5753–5766 (1997).

21. Marshall, J., Hill, C., Perelman, L. & Adcroft, A. *Hydrostatic, quasi-hydrostatic, and nonhydrostatic ocean modeling* 1997.

22. Andrews, D. G. & McIntyre, M. E. Planetary Waves in Horizontal and Vertical Shear: The Generalized Eliassen-Palm Relation and the Mean Zonal Acceleration. *Journal of the Atmospheric Sciences* **33,** 2031–2048 (1976).

23. Plumb, R. A. & Ferrari, R. Transformed Eulerian-Mean Theory. Part I: Nonquasi-geostrophic Theory for Eddies on a Zonal-Mean Flow. *Journal of Physical Oceanography* **35,** 165–174 (2005).

24. Armitage, T. W. K. *et al.* Arctic sea surface height variability and change from satellite radar altimetry and GRACE, 2003-2014. *Journal of Geophysical Research: Oceans* **121,** 4303–4322 (2016).

25. Krishfield, R. A. *et al.* Deterioration of perennial sea ice in the Beaufort Gyre from 2003 to 2012 and its impact on the oceanic freshwater cycle. *Journal of Geophysical Research: Oceans* **119,** 1271–1305 (2014).

26. Armitage, T. W. K. *et al.* Arctic Ocean geostrophic circulation 2003-2014. *The Cryosphere Discussions* **2017,** 1–32 (2017).

27. Simmonds, I. & Rudeva, I. The great Arctic cyclone of August 2012. *Geophysical Research Letters* **39,** 1–6 (2012).

28. Nurser, A. J. G. & Bacon, S. The rossby radius in the arctic ocean. *Ocean Science* **10,** 967–975 (2014).

SUPPLEMENTARY INFORMATION

A: Numerical model details

A configuration of the MIT General Circulation Model [20, 21] is employed for the numerical experiments described here. The domain is a 1200x1200 km by 800 m box with 4 km horizontal resolution and 40 levels in the vertical, most of them near the surface to resolve the developing halocline. The Rossby deformation radius in the model is $\approx$ 15 km, consistent with characteristic values of the Beaufort Gyre [28]. Therefore, the model can be considered eddy resolving and is thus able to reproduce both the eddy and the ice-ocean governor processes.

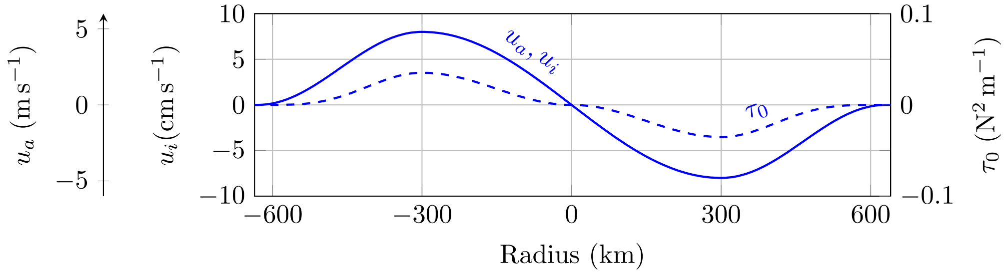

Figure A.1. Forcing profile for the wind and ice driven model experiments (solid line) and equivalent surface stress (dashed line). In the ice driven case, the surface stress is for the ocean at rest.

All simulations begin with the ocean at rest, and salinity linearly increasing from S = 34 at the surface to S = 35 at 800 m; density is considered to be a function of salinity only, effectively the case in the BG, and a linear equation of state is used. The ocean is spun up by time-invariant axisymmetric, anticyclonic, wind and ice velocity profiles shown in Figure A.1, and surface stress is computed from velocity using the equivalent of equation (1) with $\alpha = 0$ or 1 over the entire domain. The stress remains constant in the wind-driven scenario $\alpha = 0$, but is reduced by the increasing ocean surface velocity in the ice-driven scenario $\alpha = 1$. Surface salinity is relaxed to a target value of $S = 27$ during the spin up process, and bottom salinity to $S = 35$, consistent with BG observations. The wind and ice velocities are within the range of observed values [11], and are chosen to produce the same surface stress when the ocean is at rest. f−plane dynamics are considered with Coriolis parameter $f = 1.45 \times 10^{-4}$ s^{-1}, and a vertical diffusion coefficient of 1×10^{-3} m^2 s^{-1} is used. Isopycnal depth anomaly is computed as the difference between the maximum and the minimum depth of the $S = 31$ isohaline over the entire domain.

B: Freshwater content

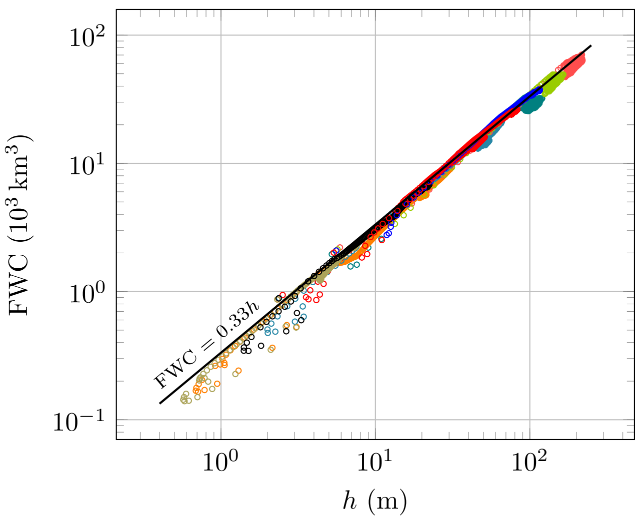

Figure B.1. Freshwater content anomaly (FWC) vs isopycnal depth anomaly for all simulations (circles) and the relationship implied by Figure 2b and Figure 3 (black line).

The freshwater anomaly for the model shown in Figure 2b and Figure 3 (right axis) is estimated as

$$FWC = \frac{S_2 - S_1}{S_2} A \sum_i h_i \tag{B.1}$$

where h_i is the $S = 31$ isohaline depth anomaly for each cell of the domain, $S_1 = 27$ is the surface salinity and $S_2 = 35$ is salinity at the bottom of the domain. This is equivalent to considering a model composed of two homogeneous layers of salinity S_1 and S_2 respectively, in accord with our analytical model and [6]. Freshwater content for all model runs is plotted against $h = \max_i h_i$ in Figure B.1.